
EXACT INVERSION FROM SPACE-FILLING TRAJECTORIES IN CONE-BEAM TRANSMISSION TOMOGRAPHY

Murdock G. Grewar[†], Glenn R. Myers[†], Andrew M. Kingston[†]

[†]Dept. Materials Physics / CTLab, RSPHys, Australian National University, Canberra, ACT 2601, Australia.

December 9, 2024

ABSTRACT

This article introduces a new theory of exact inversion in cone-beam transmission tomography where the source point locus is a 2D surface, 3D volume, or something more complex.

We specialise the theory to the case of the cylinder-shaped source locus, and we describe in detail a functioning practical implementation of the inversion algorithm for this geometry. This locus is accessible to CT scanners which include translational and rotational manipulators (e.g. typical helical scanners). This serves as a concrete instantiation of the theory and as a reference implementation which is immediately applicable to many contemporary scanning apparatuses.

We illustrate some error characteristics of the algorithm through reconstructions of a simulated dataset. We finish with a reconstruction performed on a set of experimental data acquired with a low-pitch sparsely sampled helical trajectory.

Keywords computed tomography · inverse problems · computational mathematics

1 Introduction

This article introduces a new theory and method of exact inversion in cone-beam transmission tomography which is applicable when the locus of X-ray source points is densely sampled from a multidimensional surface in 3D space. It is often then possible to choose a volumetric weighting which can be applied to the backprojected transmission data such that the resulting backprojection appears to come from a parallel-beam geometry. In this manner, the inversion problem is reduced to that of a parallel-beam geometry. The exact inverse then amounts to a volume convolution (a.k.a. ‘Fourier filtration’) of the weighted backprojection.

The earliest exact¹ inversion theories in transmission CT were based on the Radon transform [14, 3, 4, 5, 7]. Subsequently, various inversion theories for cone-beam XCT were published for scanning trajectories involving 1-dimensional helix-like source point loci [16, 10, 9, 18]. These theories require the projection data to be differentiated with respect to the parameter of the 1-dimensional curve (e.g. along the helix). Because of this, the source points must be finely sampled along that curve. However, there are practical limitations on the total number of radiographs that can be taken during a scan. Con-

sequently, helix-like curves used in these exact methods must be given an adequately large pitch so that the limited number of source points approximates a continuous 1-dimensional locus, enabling differentiation along that locus. Therefore, the source points of the trajectory will not well cover the range of possible views of the object. This is not ideal: the view from adjacent projections is very similar, and so the mutual data independence between radiographs is low. Furthermore, regions of the object will be constructed with differing resolution depending on their proximity to the source locus [17].

These issues are mostly remedied by relaxing the constraints on the source trajectory, allowing the source points to be distributed sparsely around the object as a multidimensional locus in what we call a *space-filling trajectory* (SFT). This enables higher quality reconstructions with fewer projections due to greater data independence between radiographs, with the drawback that the reconstruction cannot be performed exactly/directly with existing theories of inversion. A salient example is the SFT introduced by A. Kingston *et al.* [11], the locus of which approximates a 2-dimensional cylinder. This SFT has been in use at the ANU CTLab for several years, with reconstructions performed iteratively. Another way to construct SFTs is with so-called low-discrepancy sequences (LDSs) (e.g. from [12]), of which we provide an example in this article. LDSs are appealing for dynamic tomography be-

¹Exact contrasts with *iterative* methods which may be constructed from approximate inverses.

cause the angular distribution of projection data can be made uniform at a range of time-resolutions of reconstruction (e.g. see [13] for a low-discrepancy circular trajectory).

In this article, we introduce a theory of inversion which allows us to exactly reconstruct the volume from scanning data acquired with SFTs, including the cylindrical one in [11] and the spherical one in [1] as examples. The theory is not based on the Radon transform (it is based on a Fourier singular-value-decomposition of the parallel-beam X-ray transform derived in [8]) and the resulting algorithm does not require differentiation of measurement data along the source locus. Consequently, this inversion method can be applied to sparsely-sampled SFTs, making it very practical. This gives us the best of both worlds: exact inversion with trajectories that maximise data independence.

The article proceeds as follows:

- 2 *The Inversion Theory*
- 3 *Specialisation to the cylindrical source point locus*
- 4 *Practical discrete methods*
- 5 *Demonstrations*

This is followed by 6 *Conclusion* and the end matter.

Our algorithm has been tested on simulated and experimental data with great success, as demonstrated in 5 *Demonstrations*. For a rough sense of the computation time involved: if implemented as described in this article, the reconstruction procedure takes a comparable amount of computation time to performing 1-3 ordinary backprojections, and is highly parallelisable. Our simulations show excellent reconstruction precision near the data sufficiency threshold, approaching exactness in the limit as many source points are sampled.

2 The Inversion Theory

The inversion theory is derived in continuous space, assuming a continuous distribution of source points in 3D space.

2.1 Necessary and sufficient conditions for inversion

This theory of exact inversion is applicable to a broad variety of source loci. Typically, one would use a 2-dimensional surface surrounding the object. The algorithm may be specialised and optimised for particular surfaces; accommodating for a known distribution of source-points on that surface is then trivial. The precise formulation of the necessary and sufficient condition for our inversion technique to apply to a transmission experiment is as follows:

Let $X \subset \mathbb{R}^3$ be the set comprised of transmission source points. Let $p \in \mathbb{R}^3$ (e.g. a point within the reconstruction volume). Define $X_p \subseteq X$ as the set of source points which are visible² to p . The set of infinite lines in \mathbb{R}^3 which contain p is a copy of the real projective plane $\mathbb{R}P^2$. Define the subset

²A source point $x \in X$ is *visible* to $p \in \mathbb{R}^3$ if there exists a measurement of the line containing both x and p .

$L_p \subset \mathbb{R}P^2$ as those lines which have a nonempty intersection with X_p . We call L_p the *viewing sphere support at p* ; it is the set of *directions* from p in which source points from X may be found, either forwards or backwards in that direction. Define the *common viewing sphere support* L_V on a volume $V \subset \mathbb{R}^3$ as the intersection of L_p over all $p \in V$. Our inversion method can reconstruct on any volume V for which L_V satisfies the data sufficiency condition of Smith [15]: that for each plane in \mathbb{R}^3 containing the origin, it should also contain a line in L_V . The data collected in the transmission line $l \in L_p$ is discarded iff $l \notin L_V$.

In this article, we specialise to the choice of X as a cylinder. We also assume that the source points are uniformly distributed on that cylinder. Accommodating for a known, non-uniform distribution is trivial (one need only divide each projection by the density of the source points at the respective source position).

2.2 Technical exposition of the inversion method

The inversion method operates as follows: the common viewing sphere support L_V determines a translation-invariant point-spread function in V for the combined forward-backprojection, provided that an appropriate backprojection weighting is supplied. The point-spread function takes the form of an integral of Dirac-delta lines intersecting the origin. The inverse of the combined forward-backprojection amounts to a multiplication of the volume in the Fourier basis (a deconvolution) with coefficients that are determined from an integral transform of the density of lines L_V in $\mathbb{R}P^2$. Further detail is available in [8] regarding the deconvolution of parallel backprojections.

2.3 Less technical exposition of the inversion method

When a backprojection of measurements is performed, there is *locally*— meaning inside an infinitesimally small region of the volume— no distinction between a parallel-beam and a cone-beam. A single point in the volume does not know about the distance from which a backprojected measurement line came— on a sufficiently local scale, all that matters is the relative angle whence the backprojection originated, and its amplitude.

The ‘viewing sphere,’ L_p , of each local point p may be understood by analogy with a *planetarium*. Around each local point of the volume there is a planetarium, and the source points X_p serve as stars of light in the sky. Due to parallax, each planetarium looks different. The common viewing sphere support, L_V , is the maximal region of the sky which is ‘densely populated’ in *every* planetarium. The source points are to be sufficiently densely sampled so that the region L_V looks like a 2-dimensional object in the sky, rather than a discrete collection of stars. Then, the view from every planetarium (each point p) looks the same within the region L_V with one exception: the *density* of stars within L_V , which would appear as a different brightness profile of L_V between the planetariums. L_V represents a ‘region of the sky’ which appears densely populated with source points no matter from where in V you look out into the sky.

The brightness profile can be made the same across all planetariums by weighting the backprojections— that is, the brightness of the stars— differently at each p . Anything outside of L_V is blotted out (i.e. not backprojected), because not all planetariums see stars in those regions. The end result is that each planetarium sees precisely the same region of sky lit up— L_V — and with the same brightness profile. In other terms, the point-spread function of back-forward projection is translation-invariant, and the reconstruction may be produced by a multiplication of the Fourier components of the volume. This situation is that of a parallel-beam backprojection, which is a solved problem [8].

Our programme of inversion consists of two steps. The first is to perform a volumetrically-weighted backprojection of each source point, such that the combined weighted density of points on each viewing sphere is the same. This step emulates a backprojection from a parallel-beam geometry. The second step consists of a Fourier filtration (volume convolution) which recovers the tomogram from the parallel-beam backprojection in the manner described in [8].

3 Specialisation to the cylindrical source point locus

Though we have described the exact inversion theory in the previous section, the reader may find it unclear how to apply this in practice. In this section we show our working for a solution to the cylindrical source point locus. We compute the *volumetric backprojection weightings* and the *deconvolution filter*— these are the two ingredients of the inversion algorithm. The cylindrical case is of singularly broad appeal because cylindrical space-filling scans can be performed using most existing cone-beam X-ray apparatuses that already accommodate helical trajectories.

3.1 Formula for the volumetric backprojection weightings for a cylindrical trajectory

We will assume that measurements are taken on a rectangular detector which is oriented in a natural way, directly opposite the source point.

The number of source points per steradian, in the viewing sphere of a local point, is given by the product of:

- (1) the determinant of transformation from the unit sphere S^2 to the source point cylinder, where the transformation is determined by taking the intersection of the cylinder with the ray extending from the local point in the direction of $(\theta, \phi) \in S^2$, and
- (2) the density of source points at that intersection.

Let (z, φ) be the coordinates of the source point cylinder of radius R , and (θ, ϕ) be the spherical coordinates of a local viewing sphere. Let μ denote the density of source points per unit area of the cylinder, at the respective intersection point.

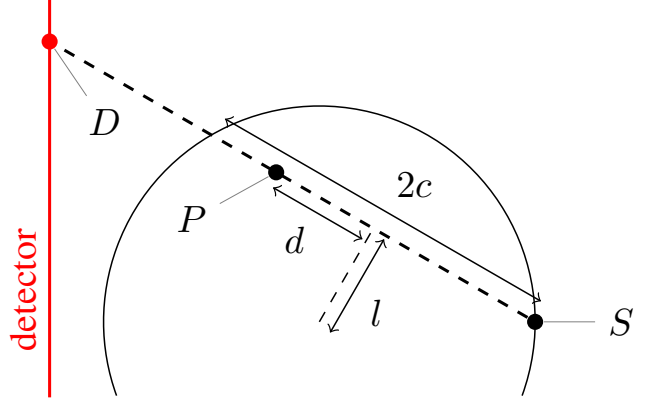


Figure 1: A diagram of the geometric quantities l, c and d which are described in 3.1 *Formula for the volumetric backprojection weightings for a cylindrical trajectory*. This is a lateral view of the cylinder, i.e. the cylinder axis goes into the page. The point S is the location of an X-ray source point on the cylinder, and P is the location of a volume point into which projection data from S is to be backprojected. The distances l, c, d and $\ell_{\pm} = |d \pm c|$ are measured in the 2D plane, as depicted. The measurement at D is the integrated attenuation coefficient along the line SD . The radiograph's weighted backprojection at P is the product of the measurement at D with the weighting (1). The polar angle θ of the line SD is invisible in this lateral view.

The solid-angular density of source points is then

$$\mu \left| \frac{R d\varphi dz}{\sin \theta d\theta d\phi} \right| = \mu R \csc \theta \left| \frac{\partial \varphi}{\partial \theta} \frac{\partial z}{\partial \phi} - \frac{\partial \varphi}{\partial \phi} \frac{\partial z}{\partial \theta} \right|.$$

Geometrically, it is easy to see that $\partial \varphi / \partial \theta = 0$, i.e., the azimuthal angle φ of the intersection point does not change with the angle of elevation of the point on the viewing sphere.³ The quantity $|\partial z / \partial \theta|$ is $|\partial (\ell \tan(\pi/2 - \theta)) / \partial \theta| = \ell \csc^2 \theta$ where ℓ is the distance in the lateral plane from the local point to the intersection point — we will dissect the expression for ℓ momentarily. It is convenient to introduce three new quantities l, c and d based on the circular chord drawn from the line extension from the local point to the intersection point on the cylinder. l is the lateral distance from the axis of the cylinder to the center of the chord. c is the half-length of the chord, in the lateral plane. d is the lateral distance from the midpoint of the chord to the local volume point. Then $\ell_{\pm} = |d \pm c|$, where the sign depends on which side of the chord the local point lies. The quantity $|\partial \varphi / \partial \phi|$ is $\frac{\ell}{R} \sqrt{1 + l^2/c^2} = \frac{\ell}{Rc} \sqrt{c^2 + l^2} = \ell/c$. The solid-angular density of source points is thus given by

$$\mu R (\csc \theta)^3 \ell^2 / c.$$

For one of the intersection points of the chord, $\ell^2 = \ell_+^2 = (d + c)^2$, while for the other it is $\ell^2 = \ell_-^2 = (d - c)^2$. To

³For a proof, imagine a top-down view of the cylinder. The angle θ makes no difference to this picture, but φ can be measured in this picture.

find the backprojection weighting, we take the multiplicative inverse of the mean of the contributions from each of the two oppositely oriented source point densities. We also assume, for the purpose of this article, that μ is a constant, meaning that the source points are distributed with uniform density on the cylinder. The resulting weighting is

$$\frac{1}{\mu R^2} (\sin \theta)^3 \frac{(c/R)}{(c/R)^2 + (d/R)^2}, \quad (1)$$

where μ is the (constant) density of source points per unit area of the cylinder of radius R , θ is the polar angle of the source point with respect to the local spherical coordinate system of the volume point, c is the half-length of the circle chord formed by projecting onto the lateral plane the line containing the volume point and the intersection point, and d is the distance from the midpoint of that chord to the volume point, also measured in the lateral plane.

The weighting (1) applies equally well *outside* the cylinder as it does inside, which is necessary for a correct backprojection weighting (because the filtration is a global operation). It assumes that backprojections from source points are computed in the forward- and backward-cone.⁴ Most cone-beam reconstruction algorithms have an existing volumetric weighting in the backprojection step, e.g. a $1/r$ or $1/r^2$ dropoff from the source point. Our weighting is to *replace* any existing weighting. The backprojection is performed within the entire padded domain, e.g. it should not terminate at the position of the detector, nor should it be restricted to reside within some cylindrical domain.

A rectangular sensor corresponds, of course, to limited horizontal and vertical angles of (back)projection. The object being scanned is required to fit within the reconstruction support, which is the cylinder of radius $R \sin(\Omega_h/2)$, where Ω_h is the full horizontal cone angle⁵. As for the vertical angle: the middle of the sensor subtends a larger vertical angle than the edges, as measured from the source point. The theory requires that all local volume points receive backprojections from the same range of angles, so we must black-out the middle-top and middle-bottom of the rectangular sensor such that the remaining data spans a constant vertical angle Ω_v . This is identical to

⁴It is also possible to use an alternate scheme where the backward-facing backprojections are flipped in sign (so that they are negative), and in this case the weighting must be changed by taking $(\ell_+^2 - \ell_-^2)/2$ when outside the cylinder of radius R , instead of $(\ell_+^2 + \ell_-^2)/2$. However, when generalising our approach to non-cylindrically symmetric trajectories, one finds that such a scheme demands that one numerically compute the quotient of arbitrarily small numbers. Therefore, the choice of scheme with $(\ell_+^2 - \ell_-^2)$ must be appropriately numerically stabilised. In our tests on cylindrically-symmetric trajectories, which do not require stabilisation because the expressions can be analytically simplified, we have not noticed any appreciable difference in the reconstruction outcome between schemes. We have not conducted any rigorous study of the differences in reconstruction outcomes between these and other possible weighting schemes.

⁵ Ω_h is measured as the angle subtended by the middle horizontal line of the detector, from the source point. A negligible amount of extra space should be reserved in the reconstruction domain for the purpose of softening (downweighting) the backprojection lines originating from the horizontal extremities of the detector.

the Colsher window [2]. Apart from this, there is no constraint on the vertical cone angle, e.g. we have performed reconstructions from simulated data with vertical cone angles as large as 170 degrees without issue.

3.2 Formula for the deconvolution filter

With the weighted backprojection performed, there is a density of samplings on the viewing sphere of each local volume element which is the same across all volume elements, i.e., shift invariant. That emulates the backprojection of a parallel-beam experiment. From here, we apply the theory of *M. Grewar* regarding the singular value decomposition of parallel-beam X-ray experiments [8]; the volume is recovered by a multiplication in the Fourier domain.

The Fourier component indexed by wavevector \mathbf{k} should be multiplied by $|\mathbf{k}|/f(\mathbf{k})$, where $f(\mathbf{k})$ is the integral of the solid-angular density of source points along the great circle perpendicular to \mathbf{k} on the viewing sphere. Source densities from antipodal directions are equivalent. Our weighting in (1) ensures that the antipode-averaged weighted source density (source points per steradian) is

$$\begin{cases} |\theta_{\text{el}}| < \Omega_v/2 : & 1 \\ \text{else} : & 0 \end{cases}, \quad (2)$$

where $\theta_{\text{el}} = \pi/2 - \theta$ is the polar angle of elevation in the local spherical coordinate system of the volume point (i.e. the polar angle of elevation of the viewing direction), and Ω_v is the vertical cone angle ($\Omega_v < \pi$) admitted by the geometry of the detector. (E.g. the vertical span from the top-left to the bottom-left of the detector, if it is rectangular.) In terms of Ω_v , the Fourier multiplication factor $|\mathbf{k}|/f(\mathbf{k})$ is

$$|\mathbf{k}| \left(1 - \frac{2}{\pi} \arccos \min \left\{ 1, \frac{\sin(\Omega_v/2)}{\sin \theta_{\mathbf{k}}} \right\} \right)^{-1}, \quad (3)$$

where $\theta_{\mathbf{k}}$ is the polar angle of \mathbf{k} , which is measured from the z axis (coinciding with the axis of the reconstruction cylinder), and $\arccos : [0, 1] \rightarrow [0, \frac{\pi}{2}]$.

3.3 Imaging a tall object

This method can image a small region of a tall object provided there is sufficient ‘overscan’. Explicitly: suppose that the entire object resides in a cylinder of radius $r \leq R \sin(\Omega_h/2)$. To correctly reconstruct a region with z coordinates (along the cylinder) spanning $\pm L$ (meaning $[-L, L]$), one must use the projection data from a source point cylinder with z coordinates spanning (at least) $\pm(L + (R + r) \tan(\Omega_v/2))$ and compute the backprojection in a region with z coordinates spanning (at least) $\pm(L + 2r \tan(\Omega_v/2))$ before padding.

4 Practical discrete methods

The exact theory in 3 *Specialisation to the cylindrical source point locus* produced *volumetric backprojection weightings* and a *deconvolution filter* suitable for application to cylindrical

space-filling trajectories. However, they were derived in continuous space. They can be applied in a natural way to the discrete volume, and in the limit of infinitely many source points and an infinitely-finely-discretised volume, that will produce a fair reconstruction. In practice, it is inadvisable to apply these results without instituting deliberate measures to mitigate discretisation effects. Here we describe such measures, which we call *discretisation regularisations*, since they do not affect the reconstruction in the continuum limit.

There are three sources of discretisation:

1. Volume discretisation.
2. Detector discretisation.
3. Source trajectory discretisation.

Volume discretisation renders the filtration formula (3) invalid, because that is derived in infinite continuous space. We describe our adaptation in 4.4 and in the appendix B. The finite extent of the volume introduces the requirement for *padding*: this is described in 4.1.

Volume and detector discretisation both require the backprojection to be defined in discrete terms. We suggest that the backprojections be anti-aliased or ‘softened’ on the edges in order to avoid harsh aliased edges that may be magnified under filtration. Softening the backprojections interferes in a substantial way with the precise filtration required — we describe how we deal with this in 4.2 and the appendix A.

Trajectory discretisation also renders the theory invalid in an obvious way: one cannot treat a finite number of points on the cylinder as if it were a continuous uniform distribution. Naturally, one should choose a selection of source points which are distributed as uniformly as possible. However, uniformly distributing the source points is not enough. There remains an artefact which is caused by some voxels receiving fewer/greater numbers of backprojected radiographs due to the discreteness of the source point locus, however evenly the cylinder is sampled. To correct for this, we apply a correction to the discreteness of the trajectory in the form of *accumulated weight normalisation*, described in 4.5.

4.1 Low-pad correction

Theoretically, an infinite amount of padding of the reconstruction domain is required in order to perform this exact reconstruction. This is because the deconvolution kernel is not compactly supported, i.e. it has ‘infinite range’. A large padding increases the computation time and the memory requirements. In practice, we observed that an insufficient padding results in a low-spatial-frequency artefact which seems to be independent from artefacts arising from an insufficient number of projections. The obvious compromise is to tune the padding amount so that the low-pad error is comparable with or lesser than the error induced from a lack of projections.

We settled upon an alternate strategy that is more efficient and does not require manual tuning. We supply a fixed padding factor (10% padding on each end of each axis), and after the tomogram is produced, we perform a *low-pad correction* to re-

move the majority of the remaining error which is induced by a lack of padding. The low-pad correction term is the residual between a reconstruction with a large amount of padding and one with a small amount of padding. Because it is a low-spatial-frequency effect, the low-pad correction term can be probed at a lower resolution, making it computationally affordable.

Our low-pad correction technique is comprised of

- a weighted backprojection into a secondary volume (the lower resolution reconstruction) with voxel dimensions n times larger in each axis but with a large padding factor f_2 . This backprojection is performed in parallel with the backprojection into the full-resolution volume which has a smaller padding factor f_1 .
- performing the filtration step on the secondary volume.
- cropping the unfiltered secondary volume so that it has an identical padding proportion to the full-resolution volume.
- performing a filtration on the cropped secondary volume.
- comparing the difference between the cropped and uncropped reconstructions on the secondary volume.
- adding this difference to the full-resolution volume, via trilinear upscaling by a factor of n .

In this article, we have settled upon padding factors of $f_1 = 1.2$ and $f_2 = 2$, and on a downscaling factor of $n = 3$. We have not found need to tune these factors since fixing them.

4.2 Backprojection softening

Our backprojection softening amounts to an additional factor in (1). However, in applying any kind of softening to the backprojections, the formula for the great-circle integrals $f(\mathbf{k})$ (see 3.2) is altered. The effect is not negligible: the reconstruction is incorrect if $f(\mathbf{k})$ is not recomputed in a way which accounts for the softening. A horizontal softening (on the left and right edges of the backprojections) may be freely applied, ensuring that the object being scanned fits inside the unsoftened reconstruction support. The vertical softening must be carefully designed so that the new formulae for the integrals $f(\mathbf{k})$ can be derived in closed-form. See appendix A *Exact softening scheme* for an exact formula for softening and the adjusted $f(\mathbf{k})$.

The softening factor can be applied either to the measurements which are backprojected (since each detector site corresponds to a particular polar viewing angle θ through which it backprojects) or to the volume directly, as a part of the volume weighting. To avoid discretisation artefacts with low detector resolutions, we suggest applying the softening factor in volume space.

4.3 Conserving computer memory when caching the volumetric weightings

Optionally, the volumetric weightings may be precomputed at the beginning of a reconstruction, stored in memory (e.g. GPU VRAM), and repeatedly applied as necessary to each backprojected radiograph. It isn't necessary to cache the volume weightings in this way, but it can reduce the computation time (roughly, by a factor between 1 and 2) at the cost of increased memory usage. In this section, we describe how to conserve memory when choosing to cache the volume weightings.

The volumetric weighting factor given in (1), with or without vertical softening included, is subject to all the symmetries of the cylinder. This means that the volume weighting need only be computed once, for a single source point, and then translated/rotated as it is applied to other source points. Additionally, there are two discrete symmetries: reflection about the lateral plane containing the source point, and reflection about the plane containing the source point and the axis of the cylinder. Consequently, the volumetric weighting factor need only be computed once in one-quarter of the range of a backprojection, after which it may be stored in computer memory (e.g. GPU VRAM) and repeatedly applied to each of the backprojections. Most of the required computations are performed already as part of the (unweighted) backprojection process. The additional computational task for each voxel is a lookup in memory for the weight and a multiplication by that weight. To increase accuracy, we also apply first-order linear interpolation to the weighting array.

The volumetric weighting factor is generally slowly changing across the volume, so that for high-resolution reconstructions it may be downsampled without significant degradation in reconstruction quality.⁶ In this manner, the memory requirements of the weighted backprojection are asymptotically constant as the resolution of a reconstruction is increased.

4.4 Discretising the Fourier filtration

The theory for the Fourier filtration is derived in continuous space \mathbb{R}^3 . In practice, we work with discretised volumes that are split into a finite number of voxels. In order to apply the Fourier filtration, one may be tempted to first apply the conventional form of the discrete Fourier transform (DFT), and then multiply those discrete Fourier components according to the formula (3). However, this is mathematically incorrect and it results in high-frequency artefacts. (A similar point has been made in [19].) We dissect this matter in more detail in the appendix B. Stemming from that analysis, our recommendation (which is only an approximation) is to multiply the DFT in the naïve manner, but with the following additional factor:

$$\text{sincpi}(\xi_x) \text{sincpi}(\xi_y) \text{sincpi}(\xi_z), \quad (4)$$

where $\xi_{x,y,z}$ are the frequency components measured in *cycles per voxel length*, and sincpi is the *normalised* sinc function.

⁶The tolerance for downsampling is dependent on the relative radius of the reconstruction support with respect to the source cylinder radius R , since this determines the length scale of the weighting array.

Through various simulated test reconstructions, we find that this approximation is unreasonably effective in suppressing high-frequency artefacts that otherwise surface from the naïve application of (3) to the discrete Fourier domain. It also does not appear to introduce any new artefacts.

It is also necessary to make a correction to the zero-frequency component of the reconstruction, due to the inexactness of our discretisation of the Fourier filtration. We achieved this in an ad-hoc fashion, by sampling the top and bottom z slices of the backprojected volume, recording which voxels were 0, and using the mean value of these voxels as the 0 point after the filtration. If a portion of a tall object is being imaged (see 3.3 *Imaging a tall object*), this procedure will still work provided there is sufficient padding in the z axis.

4.5 Accumulated weight normalisation

There are reconstruction artefacts introduced by the discreteness of the source trajectory. These artefacts can appear in the volume as 'winding' or 'crosshatched' regions of low/high attenuation. These artefacts are similar in nature to those encountered in other exact reconstruction methods when an incorrect choice of windowing function is applied to the detector. However, the artefacts are qualitatively different in our case, as they are a discretisation effect. The source of these artefacts is the fact that different points in the volume receive different (weighted) totals of backprojections. This is an inevitable consequence of approximating a continuous source locus with a set of discrete source points. We describe here a procedure, *accumulated weight normalisation*, which applies to the weighted backprojection to mitigate these artefacts. The procedure ensures that all voxels receive the appropriate weighted (and softened) number of line backprojections.⁷

The procedure is outlined as follows: as the weighted (and softened) backprojection is calculated, we record in parallel another volume into which the softened weights are accumulated, the 'softweights' S_A . Each voxel is assigned a 'softweight' in S_A which counts the weighted (and softened) number of backprojection lines received by that voxel. After the backprojection is performed, it is normalised by comparing S_A with the *expected softweights* S_E which are the weighted (and softened) number of backprojection lines which would have been received if the source locus were a perfect, continuous cylinder.

S_E is computed once at the beginning of the reconstruction. It is computed by numerical integration of the weighting term (1) (multiplied by whatever horizontal/vertical softening functions are in use) over all source positions on the cylinder. S_E inherits the symmetries of the cylinder, being rotationally and translationally symmetric. Storing S_E as a 3D array would be memory-intensive and impractical. So, we exploit the symmetries and store only the $z = 0$ slice (a plane orthogonal to the cylinder axis). Thus, we store S_E as a 2D array in computer

⁷The 'appropriate' number of weighted (and softened) number of line backprojections is not the same everywhere in the volume because the detector has finite extent.

memory with the understanding that its value doesn't depend on the z coordinate.

Accumulated weight normalisation is applied to the weighted (and softened) backprojection as follows:

1. Set $S_A := S_A + \epsilon e^{-S_A/\epsilon}$, with $\epsilon = 10^{-6}$. (This removes 0s from S_A , replacing them with small positive numbers.)
2. Divide the weighted backprojection voxelwise by S_A .
3. Multiply the backprojection voxelwise by the *expected softweights* S_E .

5 Demonstrations

In previous sections, we described the theory and practical discrete methods behind our reconstruction algorithm. At last, we show test results (in 5.3) which showcase the accuracy and speed of our algorithm. We conclude with an illustration of a reconstruction performed on experimental data (in 5.4). Before that, we quantify the 'data sufficiency condition' in 5.1 and introduce the low-discrepancy trajectory in 5.2 as these are used in 5.3.

5.1 Computing the necessary number of source points

When the reconstruction domain is discretised, there is theoretically a threshold number of projections beyond which there is sufficient data to exactly reconstruct the volume. (To see this, one may think of the reconstruction problem in its most basic form as a finite system of linear equations. With enough independent equations, the solution is uniquely determined.)

We state here a rule of thumb for the required number of source points to meet data sufficiency. We make these assumptions:

- the detector is square,
- the detector has a sufficiently high pixel resolution, and
- the source cylinder is as close as possible to the object (i.e. the object's silhouette occupies the entire horizontal extent of the detector).

Under these assumptions, the number of source points should be equal to the voxel-height⁸ of the source cylinder multiplied by Λ_z with

$$\Lambda_z \geq \pi \sec(\Omega_h/2). \quad (\text{see 19})$$

The voxel-height of the source cylinder must be somewhat greater than the voxel-height of the reconstruction due to the 'overscan' requirement (see 3.3). Ω_h is the angle subtended by the middle of the detector from the source point.

Some further detail is found in the appendix C *Source point number for data sufficiency with the cylindrical source locus*.

⁸'Voxel-height' here means the height measured in units of voxel-lengths. The voxels are assumed to be cubic.

5.2 The Low-discrepancy Source Trajectory

One appealing way to manifest a space-filling trajectory is through a *low-discrepancy sequence* (LDS) of source points, producing a LDT. Low-discrepancy sequences are in some sense optimal as infinite sequences of points which uniformly spread across some continuous space. In addition to having an optimally even sampling of the space (e.g. cylinder) in the limit of infinitely many points (e.g. better than uniformly randomly generating points), LDSs also have the advantage that any contiguous subsequence of the LDS is also an LDS.

An example application is found in dynamic tomography. Scanning may proceed along an LDT, after which the reconstruction may split the 4D scan into 3D tomogram time-slices of any time resolution. All choices will use contiguous sequences of source points, and as such will evenly sample the cylinder, giving maximum data independence.

In our case, we construct a cylindrical SFT which is a LDT. The cylinder has a periodic φ coordinate and a z coordinate with finite bounds. The theory of *M. Roberts* [12] produces an optimal LDS on n -dimensional unit cubes. In order to adapt the 2-dimensional unit cube (unit square) to the source cylinder of height $h = (z_{\max} - z_{\min})$ and radius R , we parameterise the cylinder by coordinates

$$x_1 = \frac{z - z_{\min}}{\max\{h, R2\pi\}}, \quad x_2 = \frac{R\varphi}{\max\{h, R2\pi\}}.$$

The theory of *M. Roberts* is then used to generate an infinite sequence of points (x_1, x_2) in the range $x_1 \in [0, 1)$, $x_2 \in [0, 1)$. We reject any points which fall outside of the cylinder range; that is, we reject samples for which either

$$x_1 > \frac{h}{\max\{h, R2\pi\}}, \quad \text{or} \quad x_2 > \frac{R2\pi}{\max\{h, R2\pi\}}.$$

The resulting trajectory used in our simulations is depicted in fig. 2.

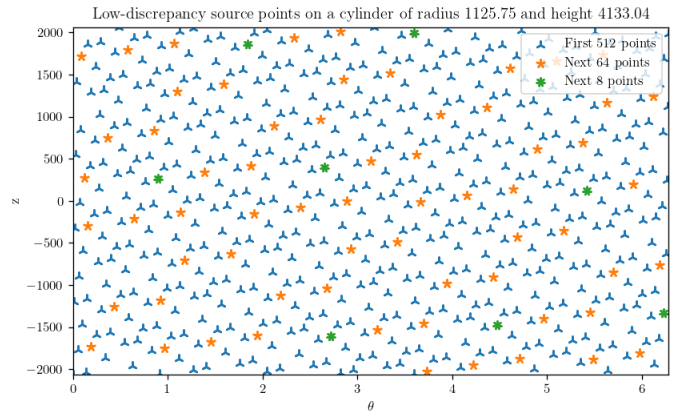


Figure 2: An illustration of a low-discrepancy trajectory (LDT). These are the first source points of the simulated projection data used in the reconstructions of figures 3 and 5.

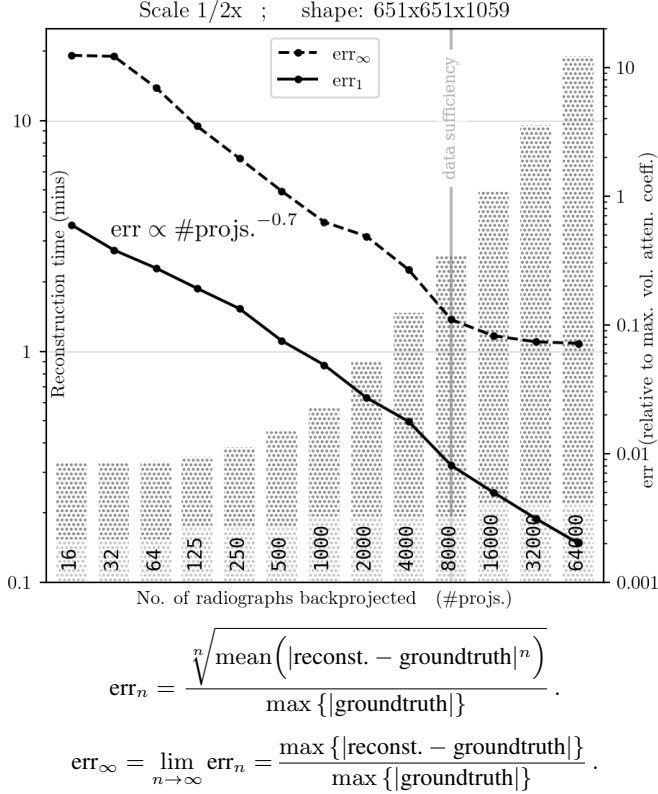


Figure 3: A graph of reconstruction time and error for the simulated dataset referred to in 5.3. The simulated volume is largely binary, consisting mostly of voxels containing either 0 attenuation or the maximum attenuation. For this reason, $\max\{|\text{groundtruth}|\}$ is almost equal to the mean attenuation inside attenuating regions of the volume. The error metrics may be intuited more meaningfully with this in mind. E.g. err_1 is the average voxel error as a proportion of the sample interior’s mean attenuation, and err_∞ is the maximum error among all voxels, as a proportion of the sample interior’s mean attenuation.

Indicated in the graph is a rough estimate of the number of projections required for data sufficiency, computed from (16). We observe a consistent power-law relationship which is approximately $\text{err} \propto (\#\text{projs.})^{-0.7}$. The same relationship was observed (only up to the data sufficiency condition) for smaller-scale reconstructions. This relationship could vary significantly for other datasets. The err_∞ reaches a floor, whereby it is dominated by the error in our discrete approximation of the Fourier filtration (see 4.4). This error reduces with larger reconstruction volumes.

The relevant hardware used for computation was: GPU: NVIDIA GeForce RTX 3090 24GiB; CPU: AMD Ryzen 9 3950X (32-core) @ 3.5GHz; RAM: 4 x 16GB DDR4 @ 3200 MT/s.

5.3 Simulations to demonstrate tomographic reconstruction time and error

To test the performance of our reconstruction algorithm, we performed a series of reconstructions on a simulated (noiseless) projection dataset consisting of 64,000 projections, each with a rectangular detector resolution of 2627×2627 pixels and a vertical cone angle Ω_v of 56.7 deg (measured as the angle subtended by a source point between the top-left to bottom-left corner of the detector). The data consisted of 32-bit floats, with a total data size of 1.7 terabytes. The scanning trajectory is the low-discrepancy trajectory (LDT) depicted in fig. 2. The projection data was generated from a discretised volume of size $1501 \times 1501 \times 2101$. In order to reduce potential projection errors arising from the discreteness of the ground truth, which may be conflated with reconstruction errors, we reconstructed at a scale of $1/2 \times$.

We reconstructed several tomograms from varying numbers of projections (we took the first n projections from the LDT, which also forms an LDT due to the properties of low-discrepancy sequences). This gives us a sense of how the algorithm performs on variously sparse/fine distributions of source points on the cylinder, approaching the continuum limit on which the inversion theory is founded. Error metrics and reconstruction times are depicted in fig. 3. In fig. 5, two arbitrary line profiles are drawn for tomographic reconstructions that used varying numbers of projections. It is fair to conclude that the reconstruction algorithm is indeed exact in the limit of a large number of projections.

We reconstructed at successively smaller scales ($1/2 \times$ down to $1/16 \times$) (not depicted) in order to probe the error characteristics in relation to the predicted sufficiency threshold from 5.1. We observed a definite shift in the error graphs at the data sufficiency threshold which manifests as a ‘flattening’ of the err_n terms with larger n . (See fig. 3 for the definition of err_n .) We also observed a strong trend in the error metrics: the reconstruction error is related to the number of projections by an approximate power law $\text{err} \propto (\#\text{projs.})^{-0.7}$ up until the predicted number of projections required for data sufficiency. This relationship will not hold for all datasets: when a reconstruction is working with insufficient projection data, it ‘invents’ the remaining data, i.e. it contains an implicit regularisation. Naturally, a regularisation will favour some ground truths and not others, similar to imposing an implicit statistical prior. For instance, we noticed the exponent -0.7 increasing (closer to 0) when we included a greater amount of non-attenuating space on the edges of the ground truth sample.

5.4 Tomographic reconstruction from experimental data

We applied our reconstruction method— except with the *low-pad correction* omitted— to an experimental micro-CT dataset acquired with the SFT of A. Kingston et al. [11]. The projection data were aligned by software before undertaking reconstruction. A slice of the tomographic reconstruction is depicted in fig. 4, with zoomed insets. On all three axes, we used a padding factor of $1.3 \times$ and a weighting array down-sampling of $2.5 \times$. This reconstruction has been performed at

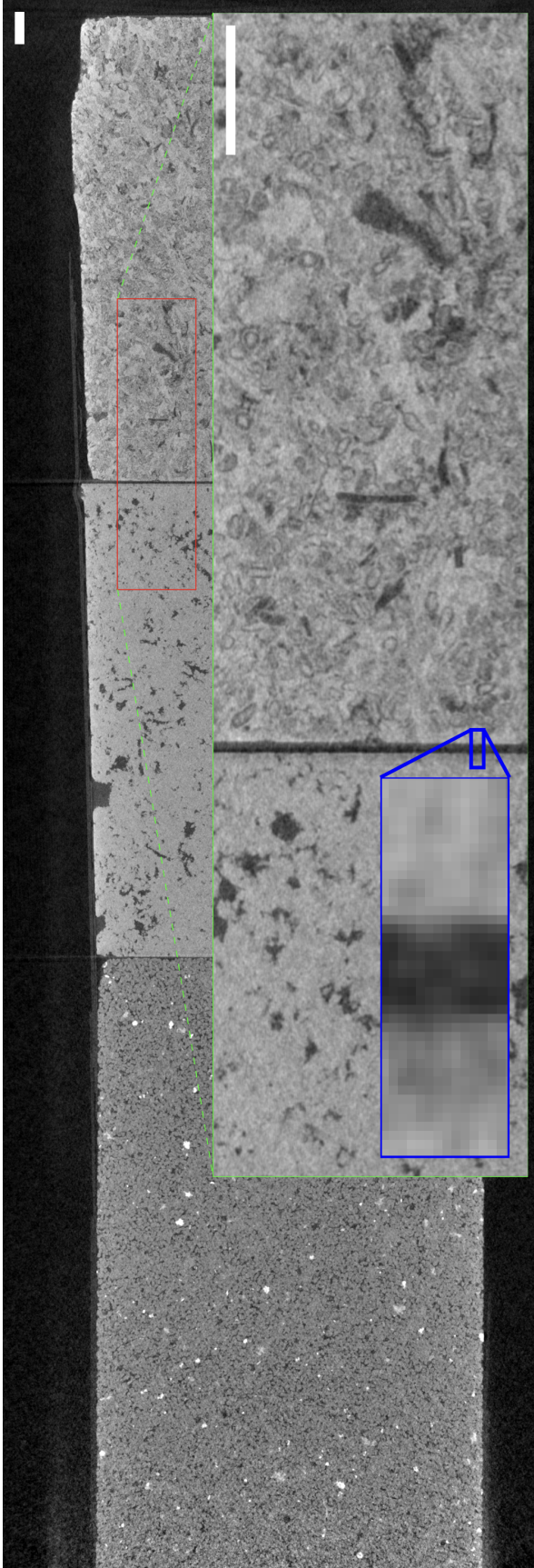


Figure 4: A recon from real data. The weighting array was downsampled by $2.5\times$. The reconstruction size is $2401 \times 2401 \times 8401$ voxels. The white scale bar is 1mm long.

a resolution which is greater than the expected resolution limit imposed by the detector. The essential geometric parameters of the scan data (which are binned down from the original detector data) are given in the following table:

detector size (pixels)	1456×1458 pixels
detector size (physical)	$\approx 405 \times 405$ mm
detector pixel size ($h \times h$)	$\approx 2.78 \times 2.78$ mm
source-to-axis distance (SA)	≈ 17.5 mm
axis-to-detector distance (AD)	≈ 433 mm
cone angle, horz. / vert.	≈ 48.4 deg / ≈ 49.4 deg
Ω_v	≈ 45.5 deg
number of source points	5930
recon size (voxels)	$2401 \times 2401 \times 8401$
recon size (physical)	$\approx 16.7 \times 16.7 \times 58.3$ mm
recon voxel size	$\approx 6.94 \times 6.94 \times 6.94$ μ m
support cylind. diameter ($2r$)	≈ 14.4 mm

The expected achievable resolution is bound by the magnification of those voxels furthest from the source (as these represent the worst-case scenario), viz.

$$(SA + r)/(SA + AD) \cdot h \approx 15.3\mu\text{m} \approx 2.20 \text{ voxel-lengths}.$$

Observing fig. 4, in the blue zoom inset, we see that the shortest transition between empty space (between the rock samples) and the inside of a rock sample is about 3 voxel-lengths. This seems to be consistent with the expected precision of 2.20 voxel-lengths, though we would have expected a somewhat finer resolution since this region is not on the edge of the reconstruction support.

However, this scan has been performed with significantly less projections than the predicted number required for data sufficiency (per (19)). At the resolution of reconstruction depicted in fig. 4, the predicted number required is in excess of 40,000. Compare this with the actual number taken, which is 5930. That the reconstruction quality appears to be bound by the detector resolution is surprising given this severe lack of projection data. The streaking artefacts (which align with the horizontal rock interfaces) are also present in a reconstruction produced with a different method, and at lower resolutions, so these artefacts appear to be related to the projection data rather than the reconstruction method. We cannot know precisely the error resulting from the source point undersampling because we don't have a 'ground truth' to compare to. However, we can glean a vague notion for what the error profile is by comparing with an analogous level of undersampling in the simulated reconstruction dataset (5.3). The projection count is deficient by a factor close to 8, corresponding to the simulation reconstruction with 1,000 projections. It is helpful to consult figures 3 and 5 respectively for associated error metrics and error line profiles. Prior to further investigation, we assume that this reconstruction from experimental data has similar error characteristics to that reconstruction, e.g., that the average voxel error is on the order of 5% of the sample interior's mean attenuation.

We also observe beam hardening artefacts in this reconstruction, and plenty of noise from measurements (these may not be easily visible in fig. 4).

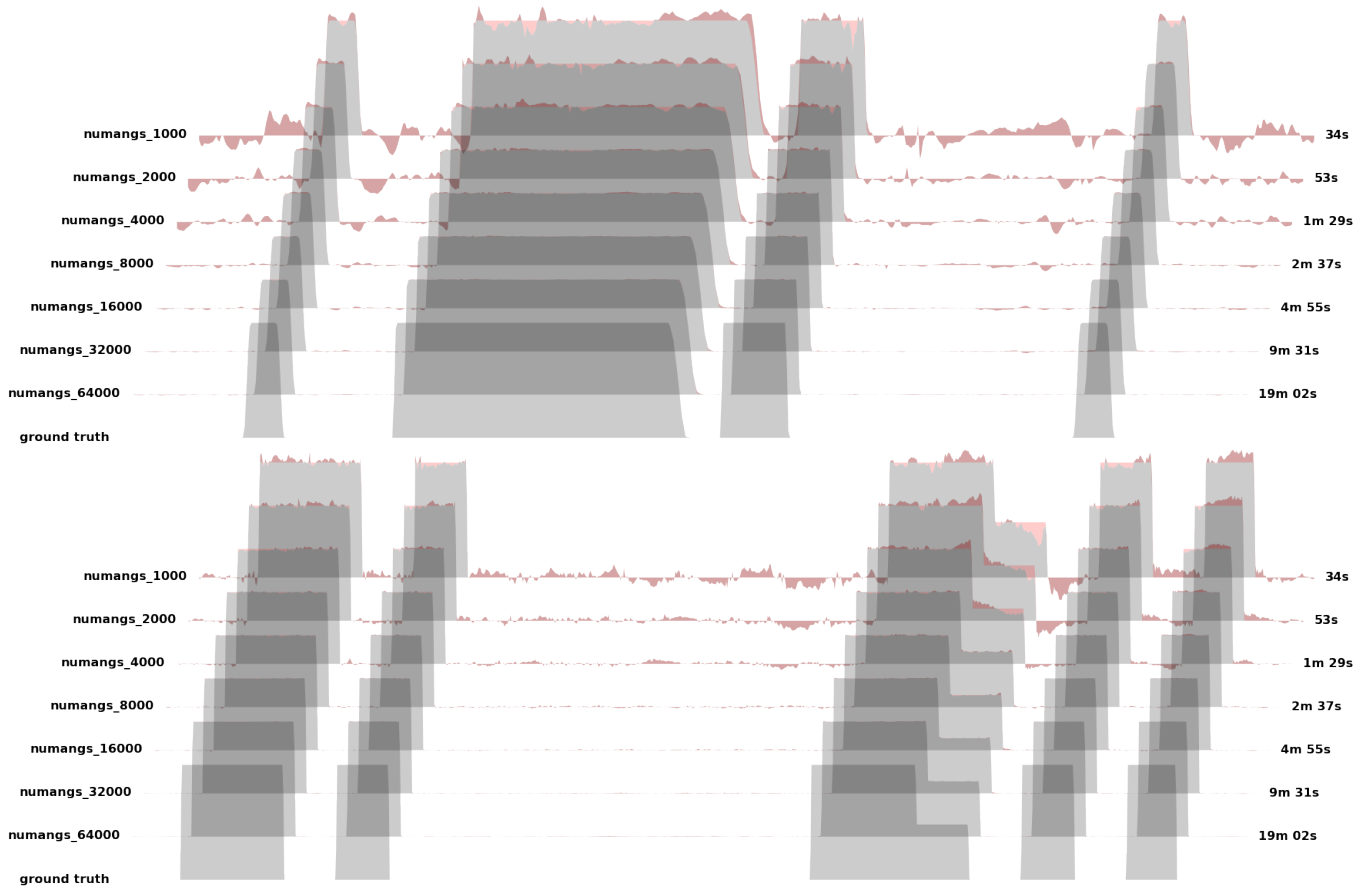


Figure 5: Arbitrarily chosen line profiles of $1/2\times$ scale reconstructions from simulated projection data. The size of the reconstructed volume is $651 \times 651 \times 1059$ voxels. We have plotted the line profiles of reconstructions using 1 000, 2 000, ... 64 000 projections, as indicated in the figure. The reconstruction times are also indicated. The reconstructions are the same as those used in fig. 3; see that figure for information about the computing hardware used. The red/pink filling highlights where the reconstruction over/underestimated the volume attenuation coefficient.

It is seen that the reconstruction approaches exactness in the limit of a large number of source points, with diminishing returns after 8000 (the number required for data sufficiency). It is interesting to note that sharp edges appear to be preserved even with significant undersampling of source points. We note that if the object being imaged has a binary attenuation coefficient, or otherwise contains a small number of distinct attenuation levels, then it may be possible to resolve the object fully with significantly less source points than dictated by the data sufficiency criterion.

This example demonstrates the ability for this algorithm to reconstruct from noisy experimental data at a high resolution, even with a significant shortfall of projection data and a large weighting array downsampling factor of $2.5\times$ in each dimension. The algorithm appears robust.

6 Conclusion

We have introduced a theory of exact inversion in transmission tomography that applies to experiments with multidimensional source loci. The theory is based on prior work by *M. Grewar* [8]. The prototypical application of the theory is to the cylindrical locus of source points. We have overcome several significant obstacles in the application of the theory to the

discrete domain, and have provided a description of an algorithm which maintains both precision and speed through its translation from the continuous theory to the discrete problem. This algorithm may be used on any cylinder-filling transmission source trajectory. Such trajectories have advantages described in the introduction to this article, and are readily accessible to most existing helical CT scanners.

The algorithm is fast and precise, as evidenced by the reconstructions on simulated data. The reconstruction on experimental data suggests that the algorithm is robust to basic experimental sources of error, and to significant projection undersampling.

Acknowledgments

Thanks to Klara Steklova for providing the experimental scanning data. This research was funded in part by an Australian Government Research Training Program (RTP) Scholarship.

A Exact softening scheme

In the body of the article, we mentioned that it is necessary to anti-alias or ‘soften’ the vertical extremities of the backprojected radiographs. The purpose of this softening is to ameliorate discretisation artefacts which otherwise surface due to aliasing. However, such softening alters the Fourier filtration, requiring that frequency component \mathbf{k} be multiplied by a coefficient which differs from its nominal value in (3). The exact multiplier for each \mathbf{k} is computed as a great-circle integral.

In this appendix, we describe a softening formula that admits a closed-form solution for the great-circle integrals. This means that the resultant combination of softening and filtration are theoretically exact, yet they do not require numerically evaluating integrals.

For brevity, we do not include a derivation, but we will describe the approach. We arrived at this formula by first writing an explicit formula for the great circle integral associated with \mathbf{k} in terms of θ_{el} and $\theta_{\mathbf{k}}$, and then noticing that the integral could be evaluated exactly if the softening function $s(\Omega_v, \theta_{\text{soft}}; \theta)$ were a polynomial in $\sin \theta_{\text{el}}$. We first chose the unique affine transformation of $\sin \theta_{\text{el}}$, termed x , which would be equal to 0 at $\theta_{\text{el}} = \Omega_v/2$ and be equal to 1 at $\theta_{\text{el}} = \Omega_v/2 - \theta_{\text{soft}}$. Then we swapped out the expression x for $3x^2 - 2x^3$ in order to make the softening function differentiable.

Here is the exact combination of softening + filtration which we devised. The softening function is given in terms of the elevation angle $\theta_{\text{el}} = \pi/2 - \theta$ by:

$$s(\Omega_v, \theta_{\text{soft}}; \theta) = \begin{cases} |\theta_{\text{el}}| \leq \Omega_v/2 - \theta_{\text{soft}} : & 1 \\ |\theta_{\text{el}}| \geq \Omega_v/2 : & 0 \\ \text{else} : & 3x^2 - 2x^3 \end{cases} \quad (5)$$

where

$$x = \gamma \sin |\theta_{\text{el}}| - \chi,$$

where

$$\gamma = (\sin(\Omega_v/2 - \theta_{\text{soft}}) - \sin(\Omega_v/2))^{-1}, \quad \chi = \gamma \sin(\Omega_v/2).$$

The associated Fourier filtration amounts to a multiplication of each Fourier component \mathbf{k} , with polar angle $\theta_{\mathbf{k}}$ measured from the axis of the cylinder, by its magnitude $|\mathbf{k}|$ and by the reciprocal of the following exact formula for the great-circle integral:

$$f(\mathbf{k}) = a + b \sin(\theta_{\mathbf{k}}) + c \sin(\theta_{\mathbf{k}})^2 + d \sin(\theta_{\mathbf{k}})^3$$

where

$$\begin{aligned} a &= 4A\chi^2(3 + 2\chi) + 4 \arcsin(\alpha) \\ b &= 24\gamma\chi(1 + \chi)(B - C) \\ c &= 6\gamma^2(1 + 2\chi)(A - \beta B + \alpha C) \\ d &= -(2/3)\gamma^3(D - 9(B - C)) \end{aligned}$$

where

$$\begin{aligned} \alpha &= \max\{0, \sin(\Omega_v/2 - \theta_{\text{soft}})/\sin \theta_{\mathbf{k}}\} \\ \beta &= \min\{1, \sin(\Omega_v/2)/\sin \theta_{\mathbf{k}}\} \\ A &= \arcsin(\beta) - \arcsin(\alpha) \\ B &= \sqrt{1 - \beta^2} \\ C &= \sqrt{1 - \alpha^2} \\ D &= \cos(3 \arcsin(\beta)) - \cos(3 \arcsin(\alpha)). \end{aligned}$$

For the avoidance of doubt, $\arccos, \arcsin : [0, 1] \rightarrow [0, \frac{\pi}{2}]$, and $\theta_{\mathbf{k}}, \Omega_v \in [0, \pi]$.

B Discrete Fourier Filtration

In 4.4 we mentioned that the Fourier filtration must be modified before it can be correctly applied to the conventional Discrete Fourier Transformation (DFT). In this appendix, we explain our thinking on this subject, and try to justify the approximation given in that section of the article.

The Fourier filtration formula (3) was derived from a consideration of the tomogram volume as a function on continuous space \mathbb{R}^3 . In practice, we represent the volume discretely, as a 3D grid of voxels. It is nonsensical to apply the continuous filtration formula (or, for example, the ramp filter) to a discrete volume. The natural resolution to this issue is to consider the discrete volume as a ‘compressed encoding’ of a continuous volume. For example, one may imagine that the discrete volume represents a continuous volume which contains regions of uniform attenuation within cubes corresponding to the discrete volume voxels. Or, one may imagine that the continuous volume represented by the discrete is produced by trilinear interpolation between neighbouring voxel centres. Whatever the case, it is helpful to think of the problem in these terms: One must...

1. make a choice about how the discrete volume should encode a continuous volume.
2. apply the continuous filter to the encoded continuous volume.
3. ‘project’ the filtered continuous volume onto some ‘nearest’ discrete-volume encoding.

We will not formalise this process. Rather, it is a helpful mental framework to follow loosely as we proceed in this analysis.

Denote the locations of the voxel centres within \mathbb{R}^3 by \mathbf{p}_i . We write the discrete volume attenuations as $f(\mathbf{p}_i) = f_i$. We imagine that the discrete volume encodes the continuous vol-

ume by a convolution of a 3-dimensional ‘comb’ of Dirac-delta distributions:

$$f = g * \sum_i f_i \delta_{\mathbf{p}_i}, \quad (6)$$

where $\delta_{\mathbf{p}_i}$ is a 3-dimensional Dirac-delta distribution with its peak at \mathbf{p}_i , and g is the convolution kernel, and $*$ is the convolution operator. For example, the kernels associated with the zeroth-order and first-order (trilinear) encodings mentioned above are given respectively by

$$g_0(\mathbf{v}) = \begin{cases} |v_x| > 1/2 : & 0 \\ |v_y| > 1/2 : & 0 \\ |v_z| > 1/2 : & 0 \\ \text{else} : & 1 \end{cases} \quad (7)$$

$$g_1(\mathbf{v}) = \prod_{i \in \{x,y,z\}} \max\{0, 1 - |v_i|\}. \quad (8)$$

The Fourier transform of the continuous volume is, by the convolution theorem, given by the pointwise-product of the Fourier transforms of the two functions which are convolved:

$$\tilde{f} = \mathcal{F}[f] = \tilde{g} \times \left(\sum_i f(\mathbf{p}_i) \tilde{\delta}_{\mathbf{p}_i} \right) \quad (9)$$

$$\tilde{f}(\mathbf{k}) = \tilde{g}(\mathbf{k}) \left(\sum_i f_i e^{-i\mathbf{k} \cdot \mathbf{p}_i} \right), \quad (10)$$

where the pointwise-product of functions is defined by $(a \times b)(x) = a(x)b(x)$. To perform the filtration in the continuous domain, we multiply \tilde{f} by the appropriate transfer function (e.g. the formula in (3), or $|\mathbf{k}|$ for the ramp filter) which we denote $\tilde{t}(\mathbf{k})$. The Fourier transform of the filtered continuous volume is

$$\tilde{t}(\mathbf{k}) \tilde{g}(\mathbf{k}) \left(\sum_i f_i e^{-i\mathbf{k} \cdot \mathbf{p}_i} \right)$$

Finally, to recover a discrete encoding of the resultant volume, we resample the resulting function at points \mathbf{p}_i , after optionally convolving it once more with a kernel h . (For example, with $h = g_0$, the voxels would inherit the integrated attenuation within their voxel. With $h = 1$, i.e. h absent, the voxels would inherit the value sampled from their centre.) Whatever the choice of g, h and whatever the transfer function \tilde{t} , the resulting expression for the filtered function in the continuous domain is

$$\tilde{y}(\mathbf{k}) = \tilde{t}(\mathbf{k}) \tilde{g}(\mathbf{k}) \tilde{h}(\mathbf{k}) \left(\sum_i f_i e^{-i\mathbf{k} \cdot \mathbf{p}_i} \right),$$

By design, the discrete samplings $y(\mathbf{p}_i) = y_i$ will be our filtered discrete volume. Computing the inverse Fourier transformation at point \mathbf{p}_j on the discretised volume, we find

$$\begin{aligned} y_j &= \iiint d^3\mathbf{k} \tilde{t}(\mathbf{k}) \tilde{g}(\mathbf{k}) \tilde{h}(\mathbf{k}) \left(\sum_i f_i e^{i\mathbf{k} \cdot (\mathbf{p}_j - \mathbf{p}_i)} \right) \\ &= \sum_i f_i \iiint d^3\mathbf{k} \tilde{t}(\mathbf{k}) \tilde{g}(\mathbf{k}) \tilde{h}(\mathbf{k}) e^{i\mathbf{k} \cdot (\mathbf{p}_j - \mathbf{p}_i)} \\ &= \sum_i f_i \mathcal{F}^{-1} \left[\tilde{t}(\mathbf{k}) \tilde{g}(\mathbf{k}) \tilde{h}(\mathbf{k}) \right] (\mathbf{p}_j - \mathbf{p}_i). \end{aligned}$$

This is a discrete convolution between f and the discrete samplings of the continuous kernel $K = \mathcal{F}^{-1} \left[\tilde{t} \times \tilde{g} \times \tilde{h}(\mathbf{k}) \right]$.

The extent of K may be infinite, such that the discrete convolution cannot be computed in a finite number of operations. However, in practice the kernel K will drop off quickly from the origin, as is our case. It is convenient for us to implement the discrete convolution as a multiplication between components of the conventional Discrete Fourier Transformations (using the discrete convolution theorem). However, multiplication of DFTs implements cyclic convolution. To account for this, an appropriate padding of 0s must be applied, extending the finite domain of f (cf. [19]). The formula for the filtration y of the discrete volume f is

$$y = \text{PDFT}^{-1} [\text{DFT}[C] \times \text{PDFT}[f]] \quad (11)$$

$$\text{where } C = \text{discretely sampled } \mathcal{F}^{-1} \left[\tilde{t} \times \tilde{g} \times \tilde{h} \right],$$

and where the symbol \times represents a pointwise multiplication between two discrete Fourier transforms, the operator DFT is the conventional discrete Fourier transform, and the operator PDFT is a conventional discrete Fourier transform preceded by a padding of its argument with 0s.

Computing the discretely sampled C is difficult due to the 3-dimensional integration over \mathbf{k} , with no immediately obvious symmetries that can be exploited to perform integration analytically, even partially. As an approximation, we may sample the $\tilde{t}(\mathbf{k}) \tilde{g}(\mathbf{k}) \tilde{h}(\mathbf{k})$ discretely, yielding the approximation:

$$y = \text{PDFT}^{-1} \left[\tilde{t} \times \tilde{g} \times \tilde{h} \times \text{PDFT}[f] \right]. \quad (12)$$

Ideally, the integrals would be computed analytically to produce an exact discrete filtration from the continuous transfer function \tilde{t} . When those integrals don’t have closed form, the above approximation may be superior to the naïve approach of sampling \tilde{t} discretely.

We have determined empirically that choosing $g = g_0$ and $h = 1$ yields significantly improved reconstructions compared with sampling \tilde{t} (from (3)) discretely: high-frequency artefacts are greatly suppressed, with no obvious introduction of new artefacts. This amounts to the following modification to the naïve discrete formula for the Fourier filtration:

From:

$$y = \text{PDFT}^{-1} \left[\tilde{t} \times \text{PDFT}[f] \right]$$

to:

$$y = \text{PDFT}^{-1} \left[\tilde{g}_0 \times \tilde{t} \times \text{PDFT}[f] \right]$$

where:

$$\tilde{g}_0(\mathbf{k}) = \text{sincpi}(\xi_x) \text{sincpi}(\xi_y) \text{sincpi}(\xi_z),$$

where the frequencies $\xi_{x,y,z}$ are measured in *cycles per voxel length*, independently from whatever length scale is used to measure \mathbf{k} , and sincpi is the *normalised sinc function*,

$$\text{sincpi}(\xi) = \begin{cases} \xi = 0 : & 1 \\ \xi \neq 0 : & \frac{\sin(\pi\xi)}{\pi\xi} \end{cases}. \quad (13)$$

C Source point number for data sufficiency with the cylindrical source locus

We have a *rough* estimate of the sufficient number of source points which is based on the Crowther criterion [6], assuming that the source point distribution is isotropic.

For smaller vertical cone angles, the Fourier frequencies which are sampled most sparsely are those in the *lateral plane*. As an approximation, we consider the number of backprojections received by a volume point from source points at all heights, at some azimuthal angle ϕ . The worst-case scenario (least source points per radian in ϕ) is at any point on the edge of the object support radius r looking in the direction tangent to the circle of radius r . We require the projection density to be such that this worst-case scenario still yields the minimum number of source points per radian. According to the Crowther criterion, that number is $D/4$ if we assume that the source points are evenly spaced, where D is the width—in voxels—of the object support diameter $2r$. However, we observe that many source points are oppositely oriented (or close to it) by coincidence, and so correspond to the same *view*. For that reason, the required number must be doubled to ensure sufficiency, i.e. we require $D/2$ source points per radian. According to this reasoning, the required density μ of source points per unit area of the source cylinder with radius R is:

$$\mu \geq \frac{1}{4Rw} \frac{r}{R} / \left(\frac{1}{2} \tan(\Omega_v/2) \sqrt{1 - (r/R)^2} \right), \quad (14)$$

where w is the width of a voxel, r is the object support radius, R is the source cylinder radius, and Ω_v is as described in 3.1.

We find that for larger cone angles, it is in fact the frequencies close to the poles $\theta_{\mathbf{k}} = 0$ and $\theta_{\mathbf{k}} = \pi$ which are least sampled, and the worst-case scenario is at points in the volume which coincide with the cylinder axis. In a similar computation to the lateral one, we find the number of source points swept out per radian of tilt in a horizontal plane, as it tilts around the axial point. We find the bound

$$\mu \geq \frac{1}{4Rw} \frac{r}{R}. \quad (15)$$

Combining the bounds, our estimate for the required number of source points per voxel-height of the source cylinder, $\Lambda_z = \mu 2\pi R w$, is

$$\Lambda_z \geq \frac{\pi}{2} \frac{r}{R} \max \left\{ 1, \left(\frac{1}{2} \tan(\Omega_v/2) \sqrt{1 - (r/R)^2} \right)^{-1} \right\}. \quad (16)$$

The source cylinder should include an ‘overscan’ as described in 3.3, so its voxel-height is somewhat greater than the voxel-height of the reconstruction.

Next, we simplify to the case where the reconstruction support radius r is taken as its maximum value $R \sin(\Omega_h/2)$, i.e., we assume that the object fills the horizontal extent of the detector. Then the required number of source points per voxel-height of the source cylinder is

$$\Lambda_z \geq \pi \max \left\{ \frac{1}{2} \sin(\Omega_h/2), \frac{\tan(\Omega_h/2)}{\tan(\Omega_v/2)} \right\}, \quad (17)$$

i.e.,

$$\Lambda_z \geq \pi \max \left\{ \frac{W}{4L \sqrt{1 + \frac{W^2}{4L^2}}}, \frac{W}{H} \sqrt{1 + \frac{W^2}{4L^2}} \right\}, \quad (18)$$

with Ω_h as described in 3.1, W the detector width, H the detector height, and L the distance from the source point to the detector. If we make the additional simplifying assumption that the detector is square, $W = H$, then the lateral bound is sharper, and (17) reduces to

$$\Lambda_z \geq \pi \sec(\Omega_h/2) = \pi \sqrt{1 + \frac{W^2}{4L^2}}. \quad (19)$$

References

- [1] Fabian Bauer, Matthias Goldammer, and Christian U. Grosse. “Selection and evaluation of spherical acquisition trajectories for industrial computed tomography”. In: *Proceedings of the Royal Society A: Mathematical, Physical and Engineering Sciences* 477.2250 (2021), p. 20210192. DOI: [10.1098/rspa.2021.0192](https://doi.org/10.1098/rspa.2021.0192). eprint: <https://royalsocietypublishing.org/doi/pdf/10.1098/rspa.2021.0192>. URL: <https://royalsocietypublishing.org/doi/abs/10.1098/rspa.2021.0192>.
- [2] James G Colsher. “Fully-three-dimensional positron emission tomography”. In: *Physics in Medicine & Biology* 25.1 (1980), p. 103.
- [3] A. M. Cormack. “Representation of a Function by Its Line Integrals, with Some Radiological Applications”. In: *Journal of Applied Physics* 34.9 (Sept. 1963), pp. 2722–2727. DOI: [10.1063/1.1729798](https://doi.org/10.1063/1.1729798).
- [4] A. M. Cormack. “Representation of a Function by Its Line Integrals, with Some Radiological Applications. II”. In: *Journal of Applied Physics* 35.10 (Oct. 1964), pp. 2908–2913. DOI: [10.1063/1.1713127](https://doi.org/10.1063/1.1713127).
- [5] A.M. Cormack. “Computed Tomography: some History and Recent Developments”. In: *Proceedings of Symposia in Applied Mathematics 1982 (Computed Tomography)* 27 (1982). DOI: [10.1090/psapm/027/692052](https://doi.org/10.1090/psapm/027/692052).
- [6] Richard Anthony Crowther, DJ DeRosier, and Aaron Klug. “The reconstruction of a three-dimensional structure from projections and its application to electron microscopy”. In: *Proceedings of the Royal Society of London. A. Mathematical and Physical Sciences* 317.1530 (1970), pp. 319–340.
- [7] Pierre Grangeat. “Mathematical framework of cone beam 3D reconstruction via the first derivative of the radon transform”. In: *Mathematical Methods in Tomography* (1991), pp. 66–97. DOI: [10.1007/bfb0084509](https://doi.org/10.1007/bfb0084509). URL: <http://link.springer.com/content/pdf/10.1007/BFb0084509>.

- [8] Murdock Geoffrey Grewar. “Quadratic Form Minimisation in X-ray Computed Tomography”. Thesis (MPhil), DOI: 10.25911/K535-9P96, URI: <http://hdl.handle.net/1885/258161>. Australian National University, Research School of Physics, Department of Applied Mathematics, 2022.
- [9] Alexander Katsevich et al. “A general scheme for constructing inversion algorithms for cone beam CT”. In: *International Journal of Mathematics and Mathematical Sciences* 2003 (2003), pp. 1305–1321.
- [10] Alexander Katsevich. “Theoretically exact filtered backprojection-type inversion algorithm for spiral CT”. In: *SIAM Journal on Applied Mathematics* 62.6 (2002), pp. 2012–2026.
- [11] Andrew M Kingston et al. “Space-filling X-ray source trajectories for efficient scanning in large-angle cone-beam computed tomography”. In: *IEEE Transactions on Computational Imaging* 4.3 (2018), pp. 447–458.
- [12] Martin Roberts. *The Unreasonable Effectiveness of Quasirandom Sequences*. 2018. URL: <https://extremelearning.com.au/unreasonable-effectiveness-of-quasirandom-sequences/>.
- [13] K Aditya Mohan et al. “TIMBIR: A method for time-space reconstruction from interlaced views”. In: *IEEE Transactions on Computational Imaging* 1.2 (2015), pp. 96–111.
- [14] J. Radon. “On the determination of functions from their integrals along certain manifolds”. In: *IEEE Transactions on Medical Imaging* 5.4 (Dec. 1986), pp. 170–176. DOI: [10.1109/TMI.1986.4307775](https://doi.org/10.1109/TMI.1986.4307775).
- [15] Bruce D. Smith. “Image Reconstruction from Cone-Beam Projections: Necessary and Sufficient Conditions and Reconstruction Methods”. In: *IEEE Trans. Med. Imaging* 4.1 (Mar. 1985), pp. 14–25. DOI: [10.1109/tmi.1985.4307689](https://doi.org/10.1109/tmi.1985.4307689).
- [16] K. C. Tam. “Exact Image Reconstruction in Cone Beam 3D CT”. In: *Review of Progress in Quantitative Nondestructive Evaluation: Volume 14*. Ed. by Donald O. Thompson and Dale E. Chimenti. Boston, MA: Springer US, 1995, pp. 657–664. ISBN: 978-1-4615-1987-4. DOI: [10.1007/978-1-4615-1987-4_81](https://doi.org/10.1007/978-1-4615-1987-4_81).
- [17] Trond Varslot et al. “Considerations for high-magnification high-cone-angle helical micro-CT”. In: *Developments in X-ray Tomography VIII*. Vol. 8506. SPIE, 2012, pp. 259–268.
- [18] Yangbo Ye et al. “A general exact reconstruction for cone-beam CT via backprojection-filtration”. In: *IEEE transactions on medical imaging* 24.9 (2005), pp. 1190–1198.
- [19] Gengsheng L Zeng. “Revisit of the ramp filter”. In: *2014 IEEE Nuclear Science Symposium and Medical Imaging Conference (NSS/MIC)*. IEEE, 2014, pp. 1–6.